



OPEN

Impact of Lorentz force on the pulsatile flow of a non-Newtonian Casson fluid in a constricted channel using Darcy's law: a numerical study

Amjad Ali¹✉, Hamayun Farooq¹, Zaheer Abbas², Zainab Bukhari¹ & Attia Fatima¹

The present paper examines the flow behavior and separation region of a non-Newtonian electrically conducting Casson fluid through a two-dimensional porous channel by using Darcy's law for the steady and pulsatile flows. The vorticity-stream function approach is employed for the numerical solution of the flow equations. The effects of various emerging parameters on wall shear stress and stream-wise velocity are displayed through graphs and discussed in detail. It is noticed the increasing values of the magnetic field parameter (Hartman number) cause vanishing of the flow separation region and flattening of the stream-wise velocity component. The study also reveals that the non-Newtonian character of Casson fluid bears the potential of controlling the flow separation region in both steady and pulsating flow conditions.

Non-Newtonian fluids have earned a lot of attention because of a wide range of their applications in science and engineering. Various models such as Jeffery fluid, elastic fluid, micro-polar fluid, and Casson fluid are termed as non-Newtonian fluids. The mechanics of non-Newtonian fluids pose challenges for scientists, engineers, and mathematicians because of their versatility¹⁻³.

Casson fluid is a non-Newtonian fluid introduced by Casson⁴. Casson fluid is a shear-thinning liquid that is supposed to have an infinite viscosity at zero shear rate, yield stress below which there is no flow and zero viscosity at an infinite shear rate⁵. This means that if the shear stress is lower than the yield stress, it acts like a solid. However, Casson fluid tends to flow as the shear stress surpasses the yield stress. Some examples of Casson fluid are Jelly, salt solutions, ketchup, paints, shampoo, tomato sauce, honey, soup, concentrated fruit juices, etc.

Human blood is assumed to have low electric conduction. It is remarkably affected by a magnetic field⁶. The phenomenon of blood flow through narrow vessels at low shear rates can be described precisely as a Casson fluid. Numerous studies have been performed regarding blood flow with varying hematocrits, blood temperature, and blood behavior as a Casson fluid⁷⁻⁹. The findings of such analyses help in the development of models such as for the blood oxygenators and haemodialysers. Sarifuddin⁹ analyzed the effects of stenosis and mass transfer on arterial flow. Siddiqui et al.¹⁰ studied blood pulsation within the stenotic artery by modeling blood as a Casson fluid and discussed how the blood flow is affected by the pulsation, stenosis, and non-Newtonian behavior. Priyadharshini and Ponalagusamy¹¹ studied the influence of MHD on blood parameters with magnetic nanoparticles in a stenosed artery.

Fredrickson¹² discussed the steady flow of a Casson fluid. Dash et al.⁵ investigated Casson fluid moving in a porous vessel. Mustafa et al.¹³ analyzed an unsteady boundary layer flow and heat transfer of a Casson fluid. They used the Homotopy Analysis Method in the study. Hayat et al.¹⁴ studied non-Newtonian fluid boundary layer flows caused by a stretching sheet. This phenomenon has several industrial applications. Pramanik¹⁵ investigated the boundary layer flow of a non-Newtonian fluid followed by heat transfer to an exponentially stretching surface in the presence of suction or surface blowing. Khan et al.¹⁶ investigated an unsteady flow of a Casson nanofluid

¹Centre for Advanced Studies in Pure and Applied Mathematics, Bahauddin Zakariya University, Multan, Pakistan. ²Department of Mathematics, The Islamia University of Bahawalpur, Bahawalpur 63100, Pakistan. ✉email: amjadali@bzu.edu.pk

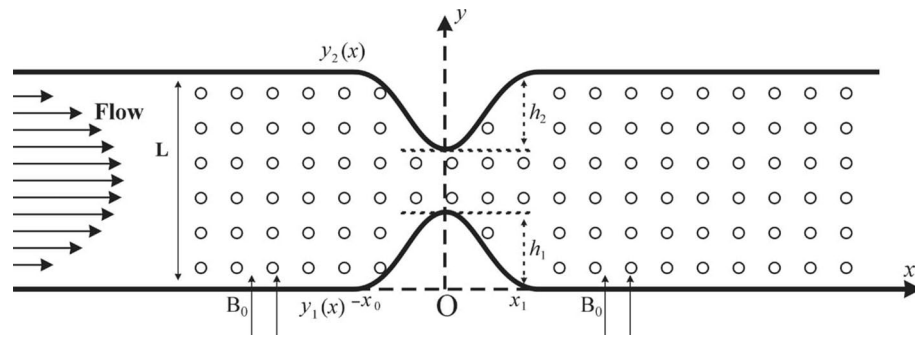


Figure 1. A schematic diagram of the flow channel with constricted walls and porous medium.

over a vertical plate with heating effects. The combined effect of Joule heating and viscous dissipation on MHD boundary layer flow and melting heat transfer of a Micropolar fluid over a stretching surface was studied by Kumar et al.¹⁷. Kumar et al.¹⁸ investigated the flow of the Marangoni boundary layer in a Casson nanofluid with the impact of a chemical reaction and the uniform effect of heat source/sink as well as convective conditions. Kumar et al.¹⁹ also investigated the Marangoni boundary layer flow over a stretching sheet in a Casson nano liquid, as well as the impact of a chemical reaction and uniform source/sink of heat.

Kumar et al.²⁰ researched Casson fluid's magnetohydrodynamic mixed convection flow over a vertical plate with the effect of Cross diffusion and nonlinear thermal radiation. Gireesha et al.²¹ studied the impact of chemical reaction on the 3D flow and heat transfer of an MHD nanofluid in the vicinity of an elastic surface plate containing gyrotactic microorganism. By considering mixed convection, Kumar et al.²² addressed the impact of viscous dissipation on the MHD flow, heat, and mass transfer of Casson fluid over a plate.

Nourazar et al.²³ investigated an MHD Casson fluid flow in a stretching/shrinking channel. Reddy et al.²⁴ investigated the concept of unsteady MHD flow over a contract cylinder of the non-linear radiative heat transfer of Casson liquid. Debnath et al.²⁵ discussed a pulsatile non-Newtonian fluid flow through a pipe. Khan et al.²⁶ studied the heat convection of a Casson fluid over a moving vertical plate in a porous medium with MHD effects and chemical reaction. Amlimohamadi et al.²⁷ numerically examined the flow of a Casson fluid through a porous constricted channel. They assumed that the resistance provided by the porous medium obeys the law of Darcy. In such a medium, the constriction is considered as another porous medium obeying the Darcy–Forcheimer system.

Studies of the magneto-hydrodynamic flow of non-Newtonian fluid in porous mediums have received substantial interest from several researchers because of their applications within the investigation of energy sources, improvement of metal, and metal alloy formation processes, and treatment of fuel detritus^{28–31}. In considering blood as Casson fluid, Ali et al.²⁸ studied the hydro-magnetic effects on blood flow in a horizontal circular duct. The present paper aims at analyzing non-Newtonian Casson fluid flow. In particular, the objective is to investigate the behaviors of steady and pulsatile flows and the flow separation region in a constricted channel, characterized as a porous medium. The fluid is assumed to be an electrically conducting fluid with low conduction. The effectiveness of the scheme is validated by computing the results by setting $D_a = 0$ and $\beta \rightarrow \infty$ and comparing these with results computed by Bandyopadhyay and Layek³².

By using the vorticity-stream function approach, the transient flow model is solved using a numerical scheme based on the finite difference method. The effects of various parameters on the axial velocity, shear stress on both the walls, streamline distribution, and vorticity distribution are observed and argued. These parameters are the magnetic number, Reynolds number, Strouhal number, Porosity parameter, and Casson fluid parameter.

The subsequent part of the article is organized as follows. “[Mathematical formulation](#)” describes and transforms the mathematical model into a solvable form. “[Results and discussion](#)” presents the results and relevant discussions. Finally, “[Conclusions](#)” summarizes the conclusions.

Mathematical formulation

We consider a non-Newtonian electrically conducting Casson fluid through a two-dimensional porous channel. The channel has constrictions on the upper and lower walls, which are placed L units apart from each other. The flow is subjected to a uniform magnetic field \mathbf{B} perpendicular to the channel walls and an electric field \mathbf{J} normal to the plane of flow. We consider a Cartesian coordinate system (\tilde{x}, \tilde{y}) such that the direction of the flow is along the \tilde{x} -axis and the direction of β is along the \tilde{y} -axis. The constrictions are spanned from $x = -x_0$ to $x = x_0$ with its center at $x = 0$, as shown in Fig. 1. It is assumed that the magnetic Reynolds number for the flow is very small, i.e., $Re_m \ll 1$.

The governing equations of the non-Newtonian fluids are highly non-linear and more complicated as compared to those of Newtonian fluids. Due to complexity, no single constitutive equation exhibiting all properties of such fluids is available. The Casson fluid model is often considered to be better than the general viscoplastic model in fitting the rheological data that is closely related to the blood flow. The rheological equation of state for an incompressible flow of Casson fluid model is as follows^{15,33,34}:

$$\tau_{ij} = \left. \begin{aligned} &2\left(\mu_B + \frac{p_y}{\sqrt{2\pi}}\right)e_{ij}, \pi > \pi_c \\ &2\left(\mu_B + \frac{p_y}{\sqrt{2\pi}}\right)e_{ij}, \pi < \pi_c \end{aligned} \right\} \tag{1}$$

where π is the product of the component of deformation rate with itself, $\pi = e_{ij}e_{ij}$ with e_{ij} being the (i, j) th component of the deformation rate, π_c is a critical value of this product based on the non-Newtonian model, μ_B is the plastic dynamic viscosity of the non-Newtonian fluid, and p_y is the yield stress of the fluid. When $\pi < \pi_c$ then Eq. (1) can be expressed as

$$\tau_{ij} = \mu_B \left(1 + \frac{1}{\beta}\right) (2e_{ij}), \text{ where } \beta = \frac{\mu_B \sqrt{2\pi_c}}{p_y} \text{ is the Casson parameter} \tag{2}$$

Thus, the equations governing the unsteady, two dimensional MHD (magneto-hydrodynamic) flow of an incompressible Casson fluid under the effect of Lorentz force are given by

$$\frac{\partial \tilde{u}}{\partial t} + \tilde{u} \frac{\partial \tilde{u}}{\partial x} + \tilde{v} \frac{\partial \tilde{u}}{\partial y} = -\frac{1}{\rho} \frac{\partial \tilde{p}}{\partial x} + \nu \left(1 + \frac{1}{\beta}\right) \nabla^2 \tilde{u} + \frac{1}{\rho} (\mathbf{J} \times \mathbf{B})_x - \frac{\nu}{k} \tilde{u} \tag{3}$$

$$\frac{\partial \tilde{v}}{\partial t} + \tilde{u} \frac{\partial \tilde{v}}{\partial x} + \tilde{v} \frac{\partial \tilde{v}}{\partial y} = -\frac{1}{\rho} \frac{\partial \tilde{p}}{\partial y} + \nu \left(1 + \frac{1}{\beta}\right) \nabla^2 \tilde{v} - \frac{\nu}{k} \tilde{v} \tag{4}$$

The continuity equation is given by

$$\frac{\partial \tilde{u}}{\partial x} + \frac{\partial \tilde{v}}{\partial y} = 0 \tag{5}$$

where \tilde{u} and \tilde{v} are the velocity components along \tilde{x} - and \tilde{y} -axes, respectively, \tilde{p} is the pressure, ρ is the density, ν is the kinematic viscosity, β is the Casson fluid parameter, $\mathbf{J} \equiv (J_x, J_y, J_z)$ is current velocity, $\mathbf{B} \equiv (0, B_o, 0)$ is the magnetic field, B_o is the strength of the uniform magnetic field, σ is electric conductivity, μ_m is the magnetic permeability of the medium. Assume that $\mathbf{E} \equiv (E_x, E_y, E_z) = (0, 0, E_z)$ denotes the electric field. From Ohm's law

$$J_x = 0, J_y = 0, J_z = \sigma(E_z + \tilde{u} B_o) \tag{6}$$

In the case of the steady flow, Maxwell's equation $\nabla \times \mathbf{E} = 0$ implies that E_z is constant. For the present study, we assume that E_z is zero. Then, Eq. (4) gives, $J_z = \sigma \tilde{u} B_o$. Therefore, $\mathbf{J} \times \mathbf{B} = -\sigma \tilde{u} B_o^2$. Hence, Eqs. (3) and (4) become,

$$\frac{\partial \tilde{u}}{\partial t} + \tilde{u} \frac{\partial \tilde{u}}{\partial x} + \tilde{v} \frac{\partial \tilde{u}}{\partial y} = -\frac{1}{\rho} \frac{\partial \tilde{p}}{\partial x} + \nu \left(1 + \frac{1}{\beta}\right) \nabla^2 \tilde{u} - \frac{1}{\rho} \sigma \tilde{u} B_o^2 - \frac{\nu}{k} \tilde{u} \tag{7}$$

To obtain the dimensionless form of the system of Eqs. (7), (4), and (5), the following quantities are introduced:

$$\begin{aligned} x &= \frac{\tilde{x}}{L}, & y &= \frac{\tilde{y}}{L}, & u &= \frac{\tilde{u}}{U}, & v &= \frac{\tilde{v}}{U}, & t &= \frac{\tilde{t}}{T}, \\ p &= \frac{\tilde{p}}{\rho U^2}, & Re &= \frac{UL}{\nu}, & St &= \frac{L}{UT}, & M &= B_o L \sqrt{\frac{\sigma}{\rho \nu}}, & Da &= \frac{\nu}{U \sqrt{k}} \end{aligned} \tag{8}$$

Here T is the period of flow pulsation, Re is the Reynolds number of the flow, St is the Strouhal number, M is the Hartman number of the flow, U is the characteristic flow velocity.

Using the quantities from Eq. (8) in Eqs. (7), (4), and (5) gives

$$St \frac{\partial u}{\partial t} + u \frac{\partial u}{\partial x} + v \frac{\partial u}{\partial y} = -\frac{\partial p}{\partial x} + \frac{1}{Re} \left(1 + \frac{1}{\beta}\right) \nabla^2 u - \frac{M^2}{Re} u - Re Da^2 u \tag{9}$$

$$St \frac{\partial v}{\partial t} + u \frac{\partial v}{\partial x} + v \frac{\partial v}{\partial y} = -\frac{\partial p}{\partial y} + \frac{1}{Re} \left(1 + \frac{1}{\beta}\right) \nabla^2 v - Re Da^2 v \tag{10}$$

$$\frac{\partial u}{\partial x} + \frac{\partial v}{\partial y} = 0 \tag{11}$$

Boundary conditions. For the steady case, the flow between two parallel plates in the presence of B_o and E_z , the equation of motion (Eq. 3) becomes

$$\rho \nu \left(1 + \frac{1}{\beta}\right) \frac{\partial^2 \tilde{u}}{\partial y^2} - \sigma \tilde{u} B_o^2 - \rho \frac{\nu}{k} \tilde{u} = \frac{\partial \tilde{p}}{\partial x} + \sigma E_z B_o \tag{12}$$

Here E_z and $\frac{\partial \tilde{p}}{\partial x}$ are constants and all the other variables depend only on \tilde{y} .

Now we non-dimensionalize Eq. (12) by using the dimensionless quantities (Eq. 8), we get

$$C \frac{d^2 u}{dy^2} - M_1^2 u = \frac{L^2}{\rho v U} \left(\frac{\partial \tilde{p}}{\partial x} + \sigma E_z B_o \right) \tag{13}$$

where $C = \left(1 + \frac{1}{\beta}\right)$ and $M_1^2 = (M^2 + Re^2 Da^2)$. Eq. (13) has the solution

$$u(y) = \frac{1}{8} \frac{M^2}{M_1^2} \left[\frac{\cosh\left(\frac{M}{2}\right) \left[\cosh\left(\frac{M_1}{2\sqrt{C}}\right) - \cosh\left(\frac{M_1}{\sqrt{C}}\left(y - \frac{1}{2}\right)\right) \right]}{\sinh^2\left(\frac{M}{4}\right) \cosh\left(\frac{M_1}{2\sqrt{C}}\right)} \right], \quad v = 0, \quad M \neq 0 \tag{14}$$

where

$$\frac{M^2 \cosh\left(\frac{M}{2}\right)}{8 \sinh^2\left(\frac{M}{4}\right)} = - \frac{L^2}{\rho v U} \left(\frac{\partial \tilde{p}}{\partial x} + \sigma E_z B_o \right) \tag{15}$$

When $M = 0$ and $Da = 0$, the inlet u -velocity takes the form:

$$u(y) = \frac{1}{C} (y - y^2), \quad v = 0, \quad M_1 = 0 \tag{16}$$

When $M = 0$ and $M_1 \neq 0$, the inlet u -velocity takes the form:

$$u(y) = \frac{2y}{A} - \frac{2\sqrt{C} \sinh\left(y\sqrt{\frac{A}{C}}\right)}{A\sqrt{A}} + \frac{2\sqrt{C} \cosh\left(y\sqrt{\frac{A}{C}}\right) \tanh\left(\frac{1}{2}\sqrt{\frac{A}{C}}\right)}{A\sqrt{A}}, \quad v = 0, \quad M = 0, \quad M_1 \neq 0 \tag{17}$$

The outlet boundary conditions are treated as for fully developed flows. For the pulsatile flow, the flow is considered sinusoidal:

$$u(y, t) = u(y) [1 + \sin(2\pi t)], \quad v = 0 \tag{18}$$

Further, $u = 0$ and $v = 0$ (i.e., no-slip conditions) are considered on the walls.

Channel wall geometry. The mathematical representation of the constricted part of the channel is

$$y_1(x) = \begin{cases} \frac{h_1}{2} \left[1 + \cos\left(\frac{\pi x}{x_o}\right) \right], & |x| \leq x_o \\ 0, & |x| > x_o \end{cases} \quad \text{at the lower wall}$$

$$y_2(x) = \begin{cases} 1 - \frac{h_2}{2} \left[1 + \cos\left(\frac{\pi x}{x_o}\right) \right], & |x| \leq x_o \\ 1, & |x| > x_o \end{cases} \quad \text{at the upper wall} \tag{19}$$

Vorticity-stream functions formulation. The dimensionless stream function (ψ) and vorticity function (ω) are defined for two-dimensional flow as

$$u = \frac{\partial \psi}{\partial y}, \quad v = - \frac{\partial \psi}{\partial x}, \quad \omega = \frac{\partial v}{\partial x} - \frac{\partial u}{\partial y} \tag{20}$$

Differentiating Eq. (9) with respect to y and Eq. (10) with respect to x then subtracting, we get

$$St \frac{\partial}{\partial t} \left(\frac{\partial v}{\partial x} - \frac{\partial u}{\partial y} \right) + u \frac{\partial}{\partial x} \left(\frac{\partial v}{\partial x} - \frac{\partial u}{\partial y} \right) + v \frac{\partial}{\partial y} \left(\frac{\partial v}{\partial x} - \frac{\partial u}{\partial y} \right)$$

$$= \frac{1}{Re} \left[\frac{\partial^2}{\partial x^2} \left(\frac{\partial v}{\partial x} - \frac{\partial u}{\partial y} \right) + \frac{\partial^2}{\partial y^2} \left(\frac{\partial v}{\partial x} - \frac{\partial u}{\partial y} \right) \right] \left(1 + \frac{1}{\beta} \right) - \frac{M^2}{Re} \frac{\partial u}{\partial y} + Re D_a^2 \omega \tag{21}$$

Using the quantities (Eq. 20), we obtain the following equations:

$$St \frac{\partial \omega}{\partial t} + \frac{\partial \psi}{\partial y} \frac{\partial \omega}{\partial x} - \frac{\partial \psi}{\partial x} \frac{\partial \omega}{\partial y} = \frac{1}{Re} \left[\frac{\partial^2 \omega}{\partial x^2} + \frac{\partial^2 \omega}{\partial y^2} \right] \left(1 + \frac{1}{\beta} \right) + \frac{M^2}{Re} \frac{\partial^2 \psi}{\partial y^2} + Re D_a^2 \omega \tag{22}$$

$$\frac{\partial^2 \psi}{\partial x^2} + \frac{\partial^2 \psi}{\partial y^2} = -\omega \tag{23}$$

Transformation of coordinates. The transformation for the coordinates is defined as:

$$\xi = x, \quad \eta = \frac{y - y_1(x)}{y_2(x) - y_1(x)} \tag{24}$$

Due to the transformation (24), $\eta = 0$ and $\eta = 1$ correspond to the lower and upper walls, respectively. Eqs. (22) and (23) are reduced to the following forms:

$$St \frac{\partial \omega}{\partial t} + u \left(\frac{\partial \omega}{\partial \xi} - Q \frac{\partial \omega}{\partial \eta} \right) + vD \frac{\partial \omega}{\partial \eta} = \frac{1}{Re} \left(1 + \frac{1}{\beta} \right) \left[\frac{\partial^2 \omega}{\partial \xi^2} - (P - 2QR) \frac{\partial \omega}{\partial \eta} - 2Q \frac{\partial^2 \omega}{\partial \xi \partial \eta} + (Q^2 + D^2) \frac{\partial^2 \omega}{\partial \eta^2} \right] + \frac{M^2}{Re} D^2 \frac{\partial^2 \psi}{\partial \eta^2} + Re D_a^2 \omega \tag{25}$$

$$\frac{\partial^2 \psi}{\partial \xi^2} - (P - 2QR) \frac{\partial \psi}{\partial \eta} - 2Q \frac{\partial^2 \psi}{\partial \xi \partial \eta} + (Q^2 + D^2) \frac{\partial^2 \psi}{\partial \eta^2} = -\omega \tag{26}$$

where

$$P = P(\xi, \eta) = \frac{\eta y_2''(\xi) + (1-\eta)y_1''(\xi)}{y_2(\xi) - y_1(\xi)}, Q = Q(\xi, \eta) = \frac{\eta y_2'(\xi) + (1-\eta)y_1'(\xi)}{y_2(\xi) - y_1(\xi)}, R = R(\xi) = \frac{y_2'(\xi) - y_1'(\xi)}{y_2(\xi) - y_1(\xi)}, D = D(\xi) = \frac{1}{y_2(\xi) - y_1(\xi)} \tag{27}$$

Moreover, the velocity components u and v become

$$u = D(\xi) \frac{\partial \psi}{\partial \eta}, \quad v = Q(\xi, \eta) \frac{\partial \psi}{\partial \eta} - \frac{\partial \psi}{\partial \xi} \tag{28}$$

The boundary conditions for ψ and ω at the walls become:

$$\psi(\eta, t) = \left[\frac{M^2 \sqrt{C} \cosh\left(\frac{M}{2}\right) \tanh\left(\frac{M_1}{2\sqrt{C}}\right)}{8M_1^3 \sinh^2\left(\frac{M}{4}\right)} \right] [1 + \epsilon \sin(2\pi t)], \quad \text{at } \eta = 0$$

$$\psi(\eta, t) = \frac{M^2 \cosh\left(\frac{M}{2}\right)}{8M_1^3 \sinh^2\left(\frac{M}{4}\right)} \left[1 - \frac{\sqrt{C}}{M_1} \tanh\left(\frac{M_1}{2\sqrt{C}}\right) \right] [1 + \epsilon \sin(2\pi t)], \quad \text{at } \eta = 1$$

$$\omega = - \left[(Q^2 + D^2) \frac{\partial^2 \psi}{\partial \eta^2} \right]_{\eta=0,1} \tag{29}$$

Here ϵ is the pulsating amplitude. For the steady flow, $\epsilon = 0$, and for the pulsatile flow $\epsilon = 1$.

Results and discussion

The numerical solutions of Eqs. (25) and (26) subjected to the boundary conditions (Eq. 29) are computed using the finite difference method. The numerical method follows a standard approach, as used by Bandyopadhyay and Layek³². The computational domain is taken as

$$\{(\xi, \eta) | \xi \in [-x_1, x_1] \text{ and } \eta \in [0, 1]\}$$

The grid points (ξ_i, η_j) , for $i = 1, 2, \dots, n$ and $j = 1, 2, \dots, m$, are obtained using the step sizes of $\Delta \xi$ and $\Delta \eta$ in ξ -direction and η -direction, respectively. A fixed step-size Δt is used to advance the solution in time. The solution at time level l is known whereas the solution at each time level $l + 1$, for $l = 0, 1, 2, \dots$, is computed. For a time level $l + 1$, firstly, Eq. (26) is solved for $\psi = \psi(\xi, \eta)$ using the central differences for the discretization of the space derivatives and the well-known Tri-Diagonal Matrix Algorithm (TDMA) for the linear system. Secondly, Eq. (25) is solved for $\omega = \omega(\xi, \eta)$ using the well-known Alternating Direction Implicit (ADI) method. For this, the time derivative is discretized using the forward/backward difference, and the space derivatives are discretized using the central differences. The resulting linear systems at each of the two half-steps of the ADI method are solved using TDMA. For ensuring the stability of the numerical scheme, the values of the step sizes are taken as follows: $\Delta t = 0.00025$ for the steady case, and $\Delta t = 0.00005$ for the pulsatile flow with $\Delta \xi = 0.05$, $\Delta \eta = 0.02$ and $Re = 700$. Although the results for the present work are computed in serial on a high-performance multicore machine, the solutions can be obtained through parallel computing to save the execution time³⁵.

Distinct fluid parameters that describe the flow characteristics, e.g., Hartman number M , Strouhal number St , porosity parameter D_a and Casson fluid parameter β are considered for obtaining the flow profiles. In the present study, we used the computational domain as, for $-10 \leq \xi \leq 10$ and $0 \leq \eta \leq 1$ is discretized by a grid of 400×50 elements by setting step sizes of $\Delta \xi = 0.05$ in ξ -direction and $\Delta \eta = 0.02$ in η -direction. Further, we consider the flow Reynolds number $Re = 700$, and the length of the constriction $2x_0 = 4$. A symmetric constriction is considered on each of the upper and lower walls at the same location with heights $h_1 = h_2 = 0.35$; hence, the channel width remains 30% of the channel width at the throat of the constriction. The time step is considered as $\Delta t = 0.00025$ and 0.00005 for steady and pulsatile flows, respectively. As the pulsatile motion is modeled by adding the sinusoidal time-dependent function $\sin(2\pi t)$ in the inflow boundary condition, the effects of flow parameters are shown for time levels $t = 0.0, 0.25, 0.50, 0.75$. These time levels at every cycle correspond to the start of the pulsating motion, the maximum flow rate, the minimum flow rate, and the instantaneous zero net flow, respectively.

The present numerical scheme is validated by comparison of the pulsatile flow results with the relevant ones obtained by Bandyopadhyay and Layek³², which discussed a Newtonian fluid without porosity effect. Figure 2

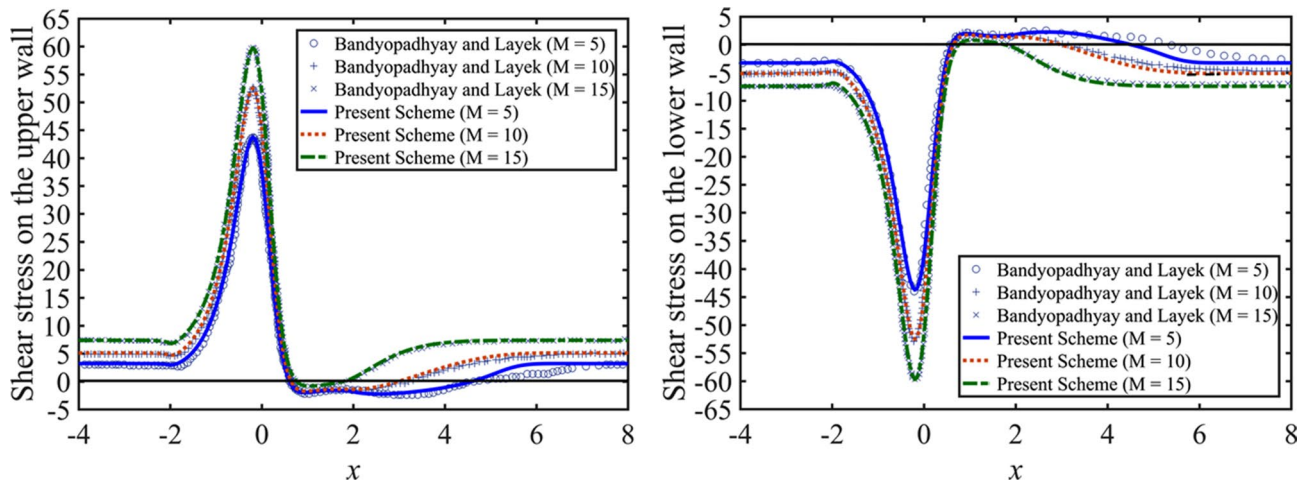


Figure 2. Wall shear stress distribution for the pulsatile flow on the upper wall (left) and the lower wall (right), for $M = 5, 10, 15$ at $t = 0.25$.

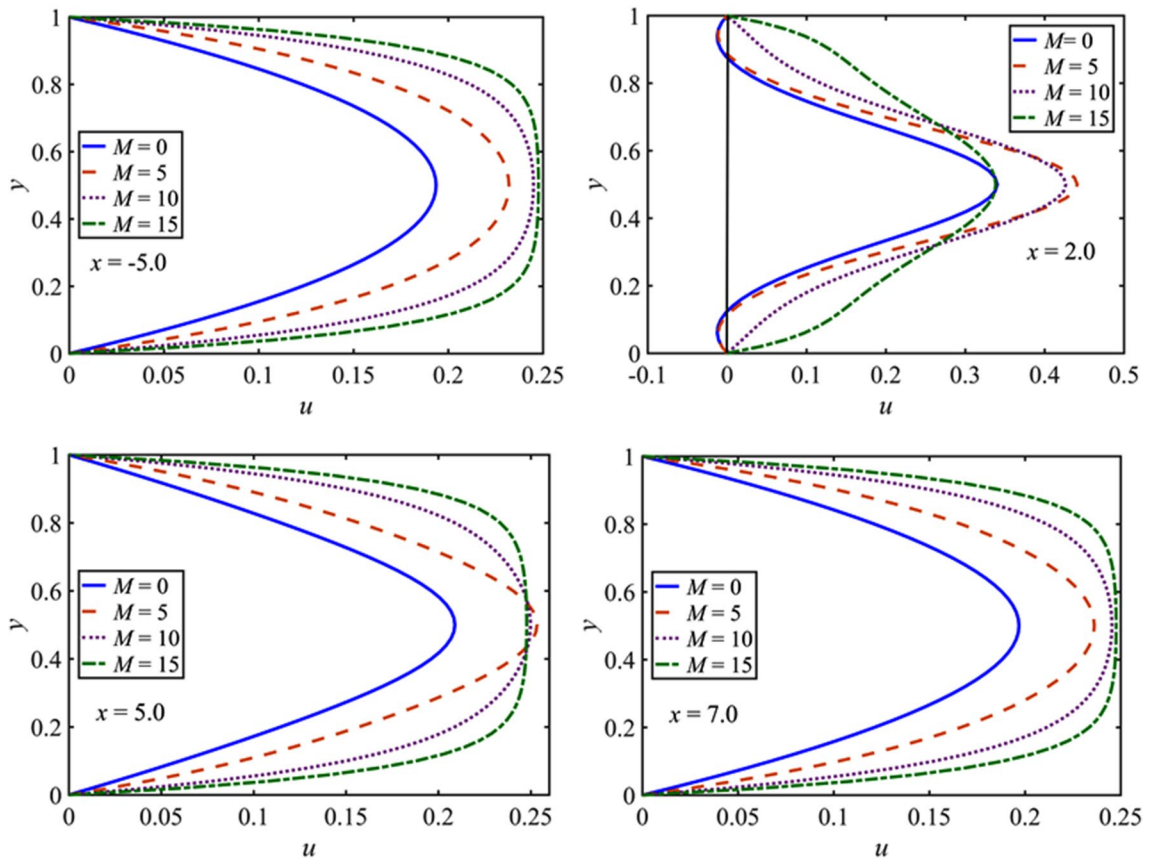


Figure 3. u -velocity profile for $M = 0, 5, 10, 15$ for $\beta = 10$ at several x values for the steady flow.

shows that there is the nearly complete agreement of the present results of wall shear stresses with those results presented by Bandyopadhyay and Layek³² for different Hartman number $M = 5, 10, 15$ at the maximum flow rate (i.e., $t = 0.25$). For the validation, the effects of the porosity and Casson fluid parameters are neglected by setting $D_a = 0$ and $\beta \rightarrow \infty$.

The variations in the stream-wise velocity component, i.e., u , in non-Newtonian fluid with $\beta = 10$ for steady flow condition at $x = -5.0, 2.0, 5.0, 7.0$ are shown in Fig. 3 for $M = 0, 5, 10, 15$. The fluid velocity u exhibits symmetric parabolic profile about $y = 0.5$ at three different locations: one before the constriction region, i.e., $x = -5.0$ and two after the constriction region, i.e., $x = 5.0, 7.0$. The u profile is also symmetric about $y = 0.5$ at the end of the constriction location, i.e., $x = 2.0$, however not parabolic. The increase in M results in a progressive flattening of u and thereby diminishing the flow separation. The peak value of u increases with M and become

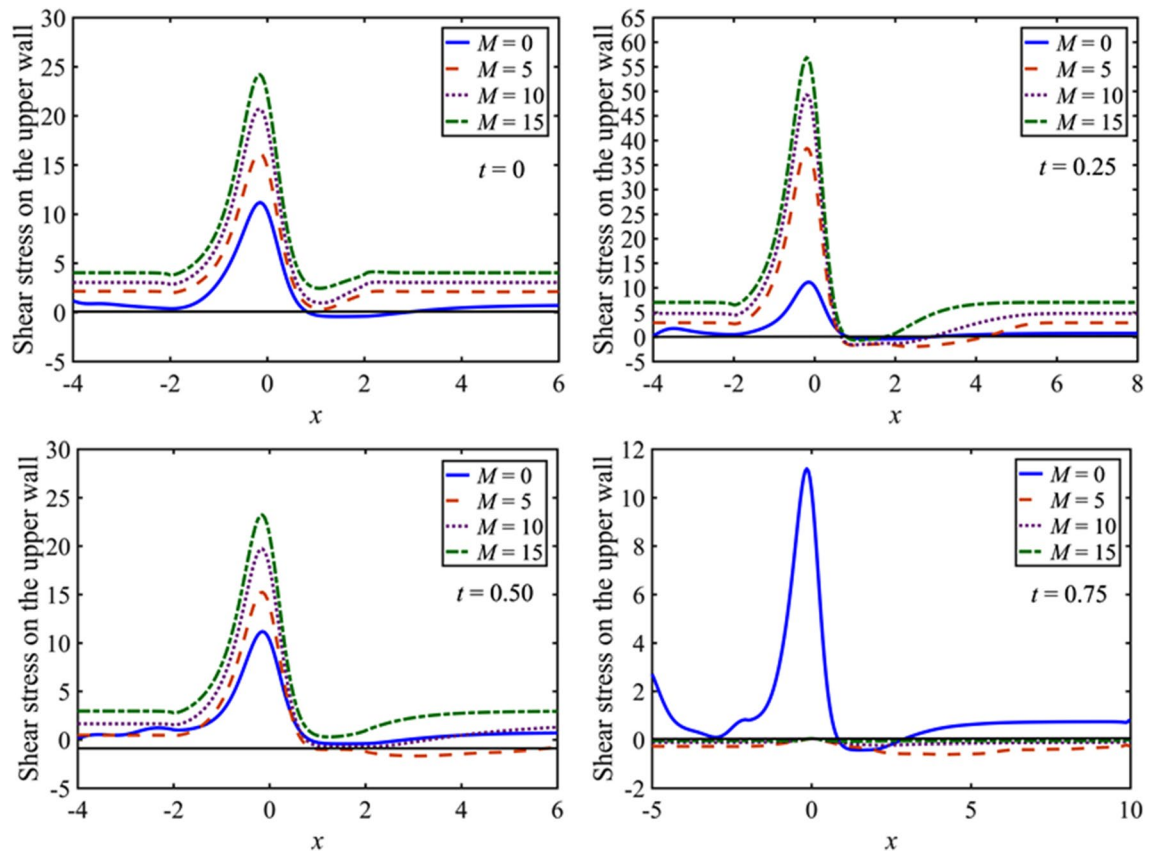


Figure 4. Distribution of the wall shear stress for $M = 0, 5, 10, 15$ and $\beta = 10$ at $t = 0, 0.25, 0.5, 0.75$.

flattered in the central region. In the upstream of the constriction, the peak values of the velocity profiles increase faster than that of the profiles in the downstream of the constriction as M increases.

The effects of M on the wall shear stress at the upper wall are shown in Fig. 4 at $t = 0, 0.25, 0.50, 0.75$ with $St = 0.02$, $\beta = 10$, and $Da = 0.002$. The distribution curve of the shear stress on the wall is significantly varying near the locale of constriction during the whole cycle. However, at the upstream of the constriction, the shear stress is linearly distributed on the wall. During the first quarter period of pulsatile time $0 \leq t \leq 0.25$, the flow is accelerating. Consequently, the peak value of the shear stress rises at the throat of the constriction and reaches its maximum at $t = 0.25$. The effects of M during this phase of time are significant. As M is increased, the shear stress on the wall increases. Further, during this phase of time, the separation region reduces with increasing M . Thus, M has a substantial impact on the shear stress for the pulsatile flow as well. In the next half period of pulsatile time $0.25 < t \leq 0.75$, the flow begins to decelerate. Consequently, the shear stress declines, whereas the flow separation region grows. The distribution of shear stress oscillates as well as alternates its sign at $t = 0.75$. This behavior is not observed during the rest of the cycle. The results at the lower wall are symmetric about the zero wall stress line to those at the upper wall.

The effects of Strouhal number on the wall shear stress at the upper wall are shown in Fig. 5 for $St = 0.02, 0.05, 0.08$ with $M = 5$, $\beta = 5$, and $Da = 0.002$. The distribution of shear stress increases with the increasing St at the start of the pulsatile motion $t = 0$, but the effects are not significant as compared to that of M where considerable variation is observed. The peak values of the shear stress coincide with the variation of St when the flow is maximum ($t = 0.25$). In the decelerating phase particularly $0.25 < t < 0.5$, the two peak values of the wall shear stress with the opposite sign are observed one is on the middle of the constriction and other is near the downstream of the constriction, further, the peak values of the wall shear stress decreasing with increasing St , when the flow rate is minimum ($t = 0.5$), but the situation is reversed and ultimately changes its sign at zero net flow ($t = 0.75$). However, the region of separation decays with increments in St and grows with time. The results at the lower wall are symmetric about the zero wall stress line to those at the upper wall.

The influence of the Casson fluid parameter (β) on the wall shear stresses are shown in Fig. 6 for $\beta = 10, 5, 1, 0.5$ with $M = 5$, $St = 0.02$, and $Da = 0.002$. The wall shear stress increases with β during a complete cycle. However, the wall shear stress distribution behaves differently not only in the different phases of a cycle but also for different values of β . The maximum peak values of the wall shear stress appear in the vicinity of the constriction ($-x_0 < x < x_0$) except for the time phase when the net flow rate is zero at $t = 0.75$. At the start of the motion ($t = 0$), an oscillating behavior of the wall shear stress is observed for large values of β equal to 10 and 5 in the upstream of the constriction ($x \leq -x_0$) and tend to be straighter in the downstream of the constriction ($x \geq x_0$). In the acceleration phase ($0 < t < 0.25$), the peak value of the wall shear stress increases,

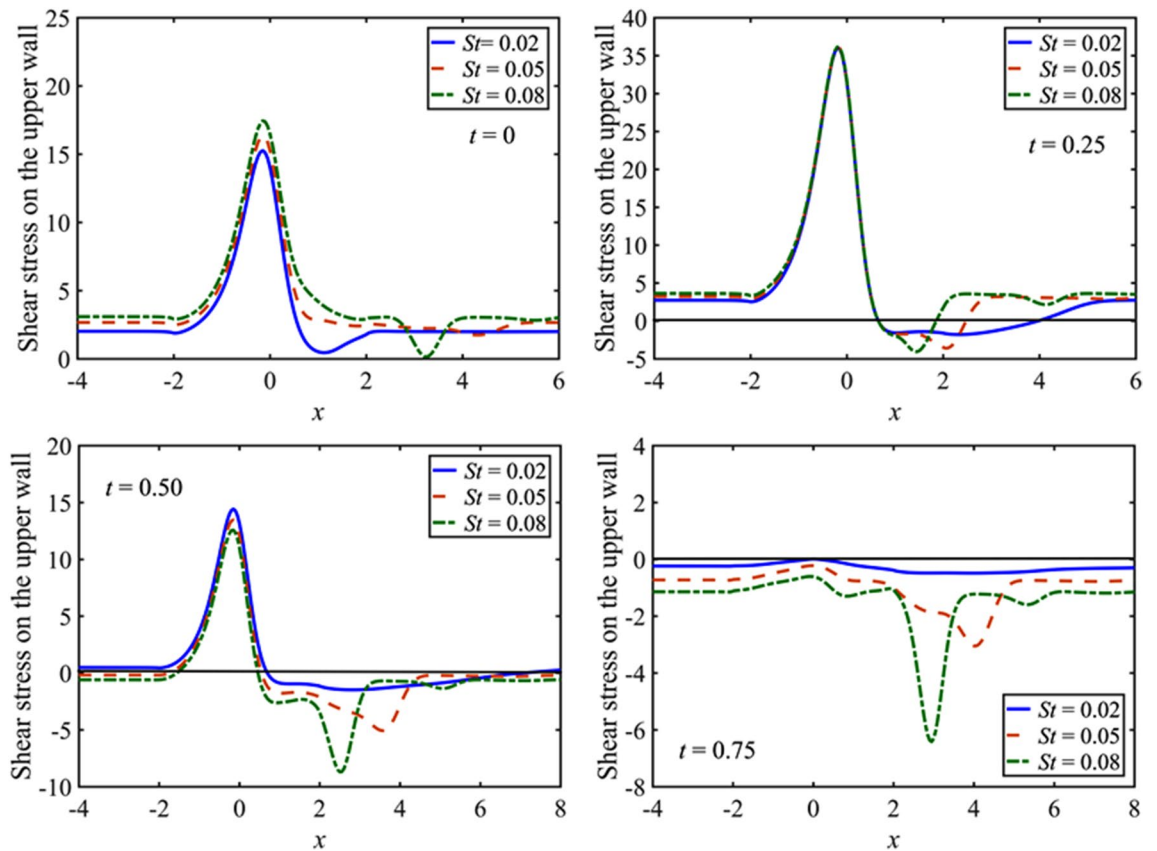


Figure 5. Distribution of the wall shear stress for $St = 0.02, 0.05, 0.08$ and $\beta = 5$ at $t = 0, 0.25, 0.5, 0.75$.

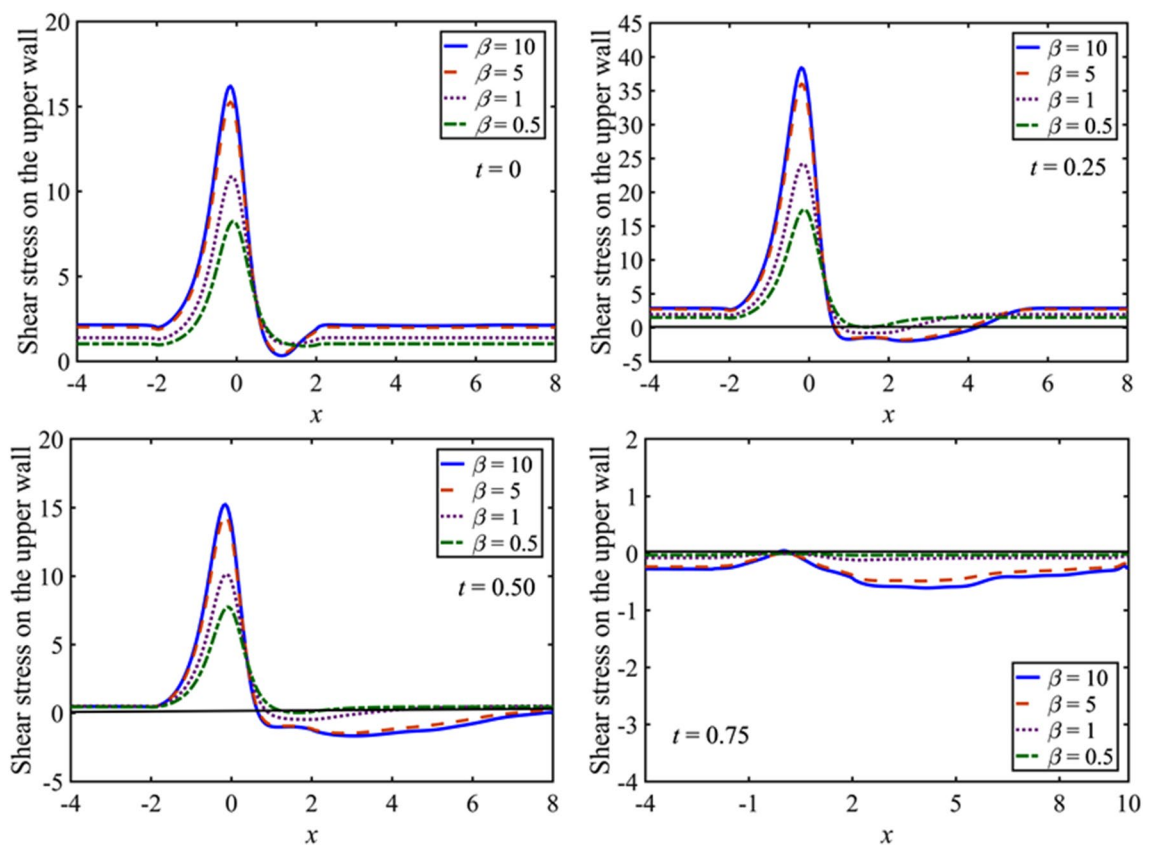


Figure 6. Distribution of the wall shear stress for $\beta = 10, 5, 1, 0.5$ at $t = 0, 0.25, 0.5, 0.75$.

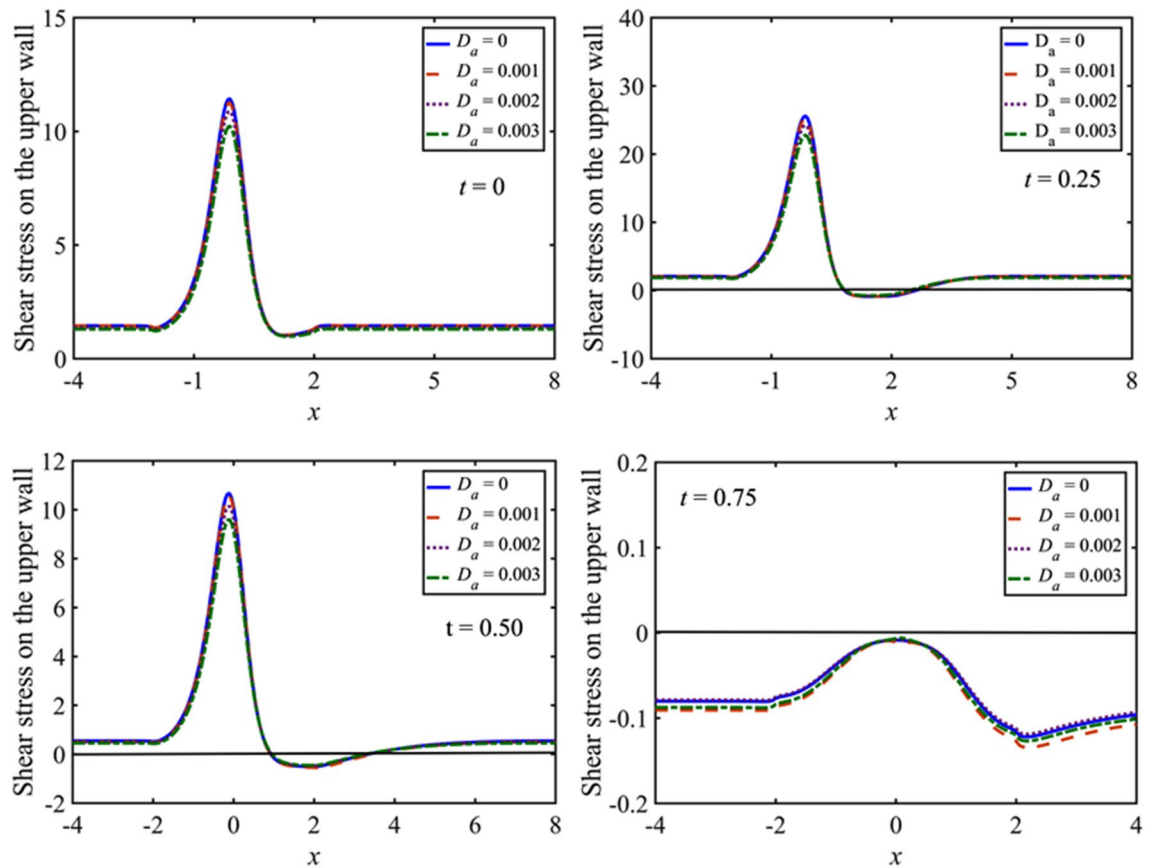


Figure 7. Distribution of the wall shear stress for $D_a = 0, 0.001, 0.002, 0.003$ with at $t = 0, 0.25, 0.5, 0.75$.

and it attains maximum value at time $t = 0.25$ for each of the values of β . Moreover, the shear stress changes its sign in the downstream of the constriction on both upper and lower walls, especially for the large values of β . For the deceleration phase $0.25 < t \leq 0.75$, the oscillating behavior of the shear stress progresses in amplitude in the upstream of the constriction for large values of β and comes to be straighter in the downstream.

The change in the wall shear stress for distinct values of porosity parameter (D_a) is shown in Fig. 7 for $D_a = 0, 0.001, 0.002, 0.003$ with $M = 5$, and $St = 0.02$. The numerical results are simulated for the small value of the Casson fluid parameter $\beta = 1.0$ to involve the effect of non-Newtonian fluid in the flow. It is noted that the peak value of the wall shear stress increases slightly with the decreasing D_a . The maximum peak values of the wall shear stress are observed at the constriction at the time when the flow rate is maximum ($t = 0.25$) and after that, the peak of the wall shear stress at the constriction decreases in the deceleration phase of the flow ($0.25 < t < 0.75$) and ultimately vanished at the time when the net flow rate is zero ($t = 0.75$).

In the pulsatile case, the profile of the stream-wise velocity component versus η at various locations $x = -5.0, 2.0, 5.0, 7.0$ in the flow field is plotted in Fig. 8. The results are shown for the magnetic parameter $= 5, 10, 15$ $St = 0.02$, $\beta = 10$, and $Da = 0.002$ at $t = 0.25, 0.5, 0.75$. Like the steady case, the stream-wise velocity u , at a particular time t , becomes flattered as M increases. However, the flow separates near the constriction at $x = 2.0$. Importantly, at $t = 0.75$ when the incoming flow becomes zero, the back-flow seems to occur near the walls. Further, the asymmetry in the flow profiles is found near the constriction for $M = 0$.

Figures 9 and 10 demonstrate the effects of M on the streamline and vorticity. The contours are shown for three different values of M with $St = 0.02$, $\beta = 10$, and $Da = 0.002$. In Fig. 9, the streamlines run smoothly over the constriction at the start of the motion ($t = 0$). However, with the start of flow acceleration, a small vortex (or bubble) appears near the walls in the lee of the constriction due to the boundary layer effects. The vortices get enlarged with time. In Fig. 10, the vortices on the walls are not the same in size and shape; a kind of asymmetric flow is found. The rotational behavior of streamlines vanishes as the value of M increases at time $t = 0$. Furthermore, the rotation of flow in the lee of constriction grows in size with time and decay with increasing M . Thus, the effect of boundary on the fluid can be controlled by applying the external uniform magnetic field. Moreover, the vorticity contours are found to be anti-symmetric with respect to the central line during the whole of a period of the pulsatile flow.

Figures 11 and 12 elucidate the variations of St on the streamline and vorticity. The contours are plotted at $t = 0, 0.25, 0.50, 0.75$ for three different values of St with $M = 5$, $\beta = 10$, and $Da = 0.002$. In Fig. 11, the streamline show smoothness over the constriction at the start of the motion ($t = 0$). However, as the flow starts to accelerate, a small vortex (or bubble) appears near the walls in the lee of the constriction, and the size of vortices increases with time; a kind of similar behavior of streamlines are found as that is noted for different value of M .

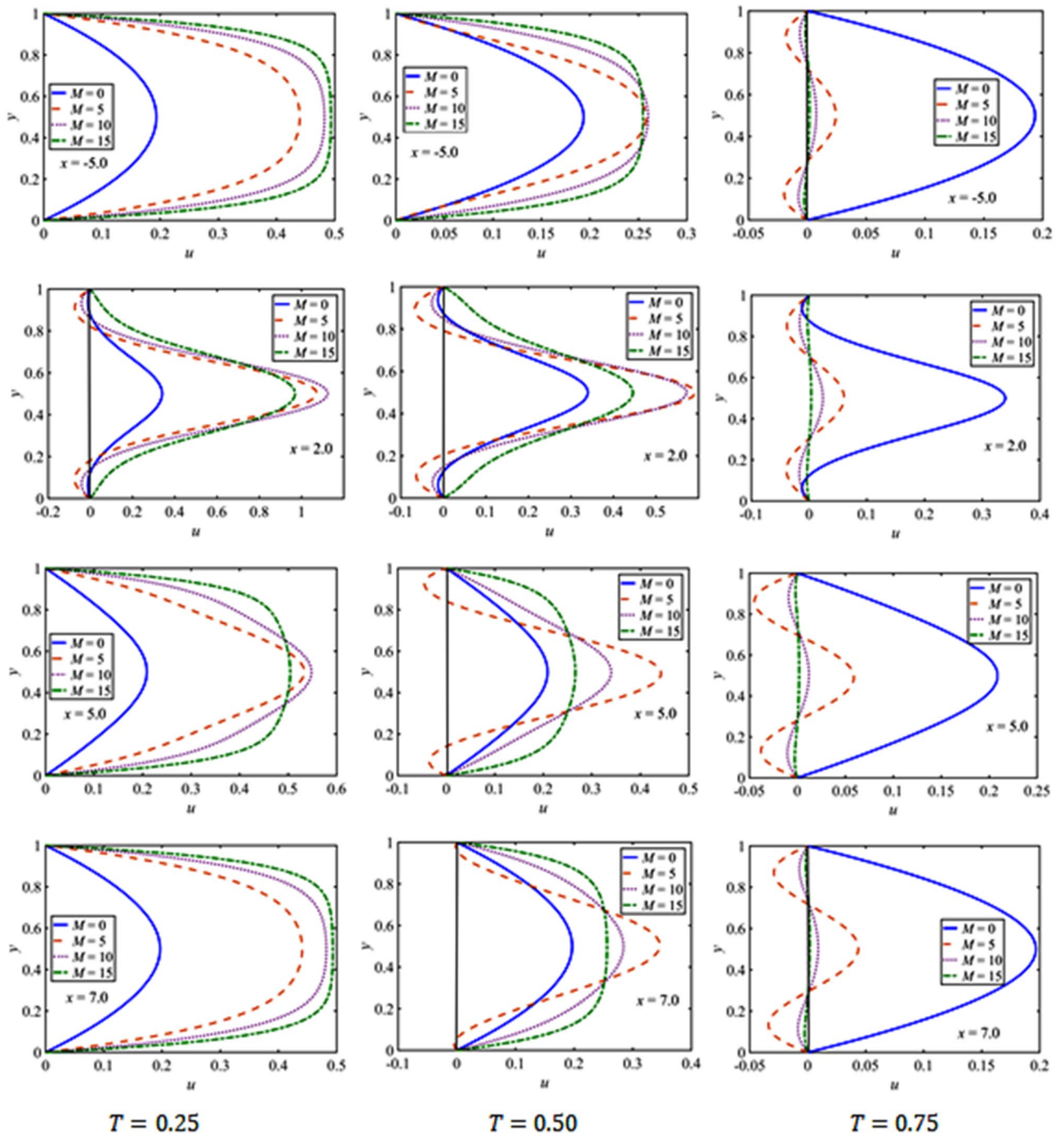


Figure 8. u -velocity profiles in the pulsatile flow at $t = 0.25, 0.50, 0.75$ against M at several x values.

In Fig. 12, as St increases, the size of the vortices reduces, and the shape becomes the same on the upper and lower walls. This indicates that the flow becomes symmetric as the value of St increases. Thus, St has significant effects, similar to M , on the flow characteristics.

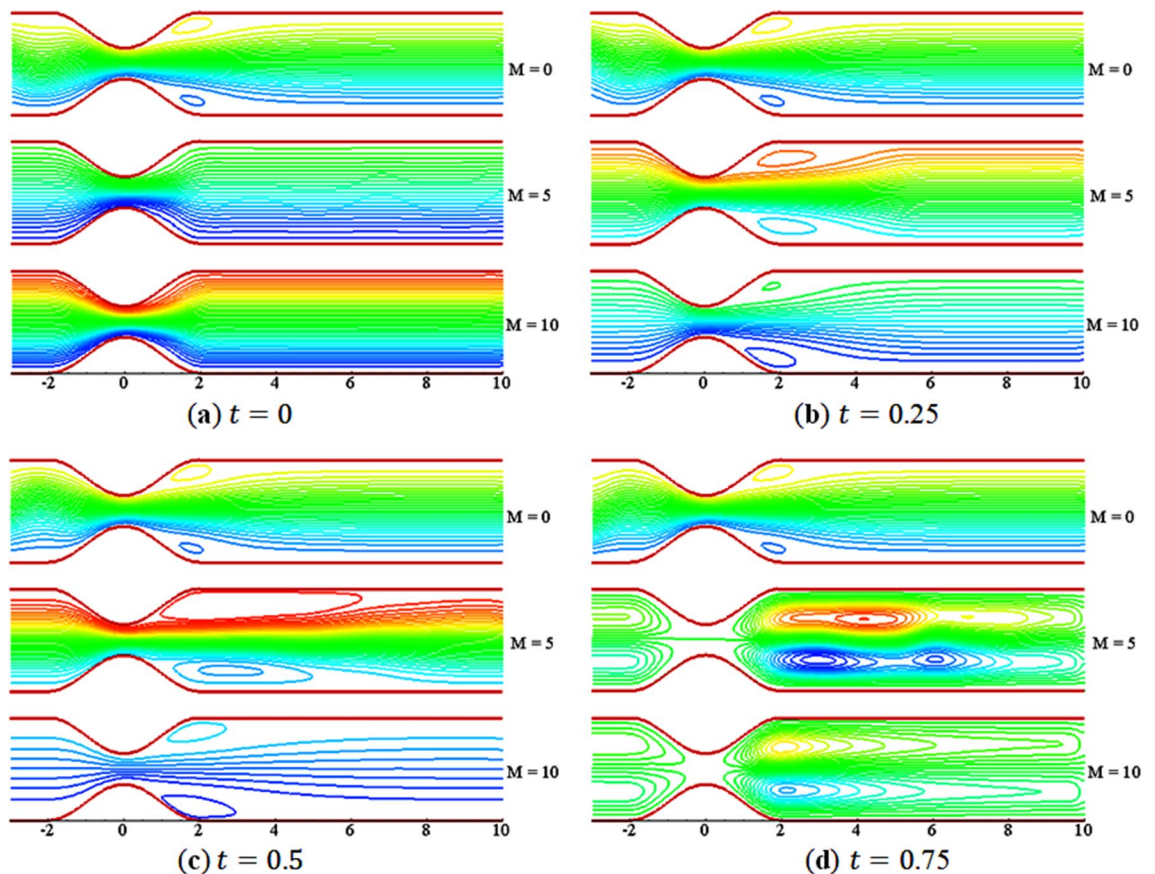


Figure 9. Streamlines contours for $M = 0, 5, 10$.

Conclusions

The impact of Lorentz force on the pulsatile flow of a non-Newtonian Casson fluid in a constricted channel using Darcy's law is numerically studied. The effects of varying the values of the Hartman number M , Strouhal number St , Casson fluid parameter β , and porosity parameter D_a on both the walls are studied. The main results of the present analysis can be listed below as:

- The peak value of the shear stresses on walls increases with time and reaches its maximum value when the incoming flow is maximum. At the start of motion, the boundary layer effects reduce with increasing M . Thus, the magnetic field parameter M significantly affects the shear stress on the walls and results in smoother flow even in the throat of constriction. However, the effects of the boundary layer continue to grow during the pulsatile flow. The boundary layer effects are higher at the minimum flow rate.
- The peak value of shear stresses on the walls increases with St with the flow acceleration. The peak values of shear stress on walls coincide with the variation of St when the flow is at a maximum flow rate. After this time period, the two peak values of shear stresses with opposite signs are observed, but the situation is reversed and ultimately changes its sign when the incoming flow becomes zero. However, the region of separation increases with time and decreasing with St .
- The peak value of shear stresses increases with the increasing β during a complete cycle.
- Increment in the value of M results in smoothing down of the streamlines in the pulsatile flow. Thus, the effect of boundary on the fluid can be controlled by applying the external uniform magnetic field.
- St has a significant impact on the contours, similar to that of the case of varying M .

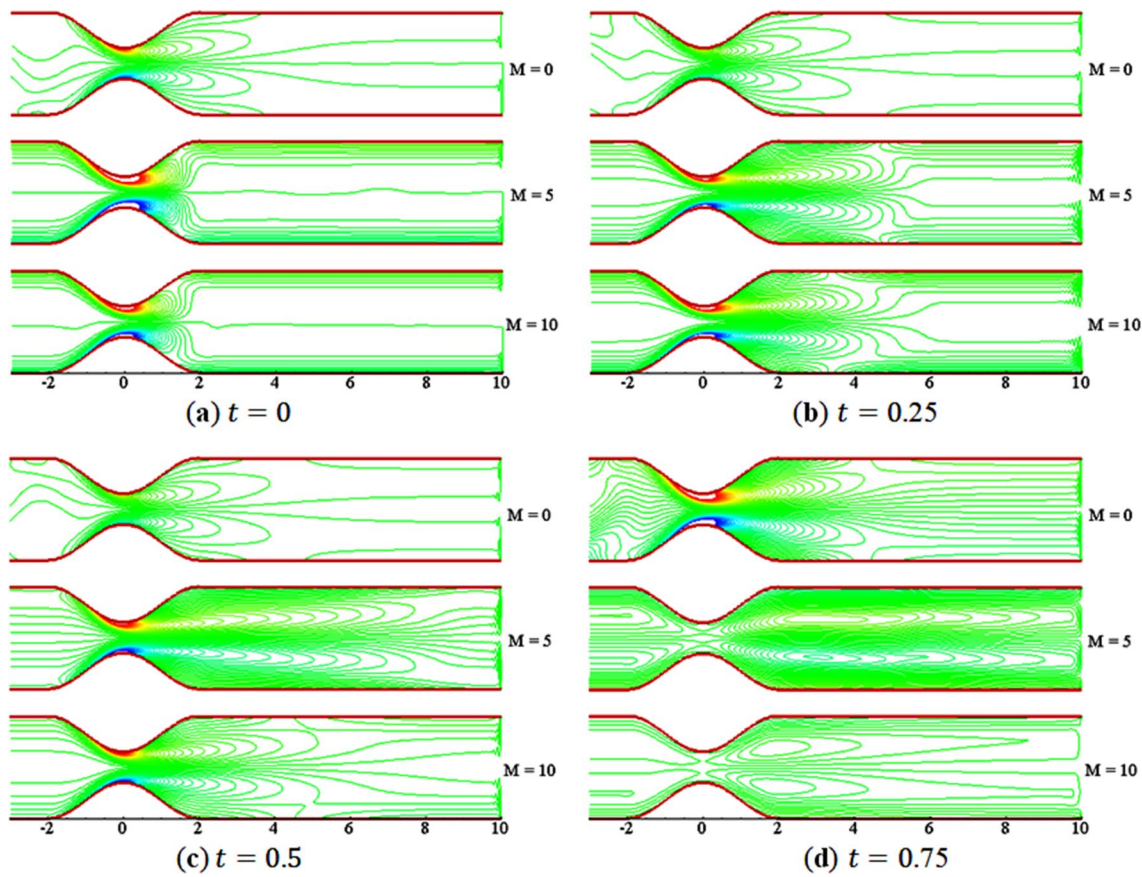


Figure 10. Vorticity contours for $M = 0, 5, 10$.

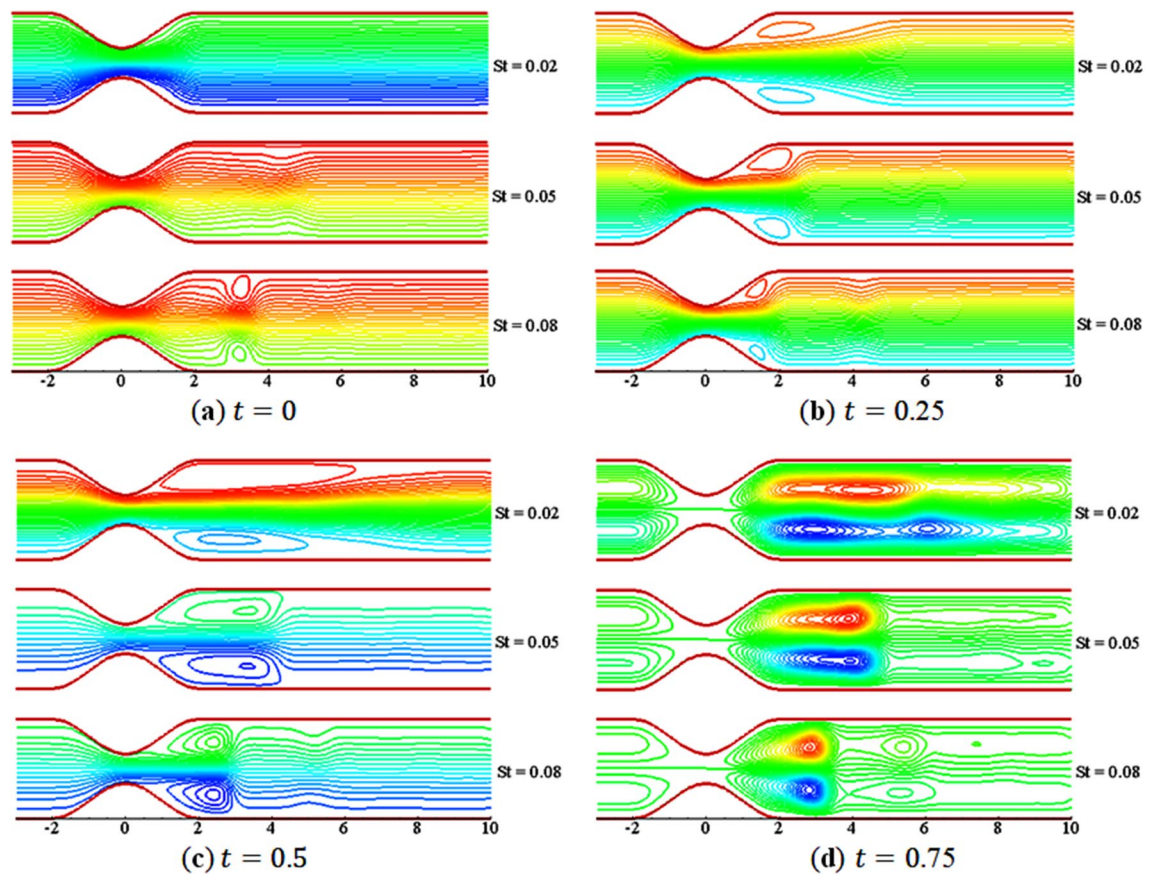


Figure 11. Streamlines contours for $St = 0.02, 0.05, 0.08$.

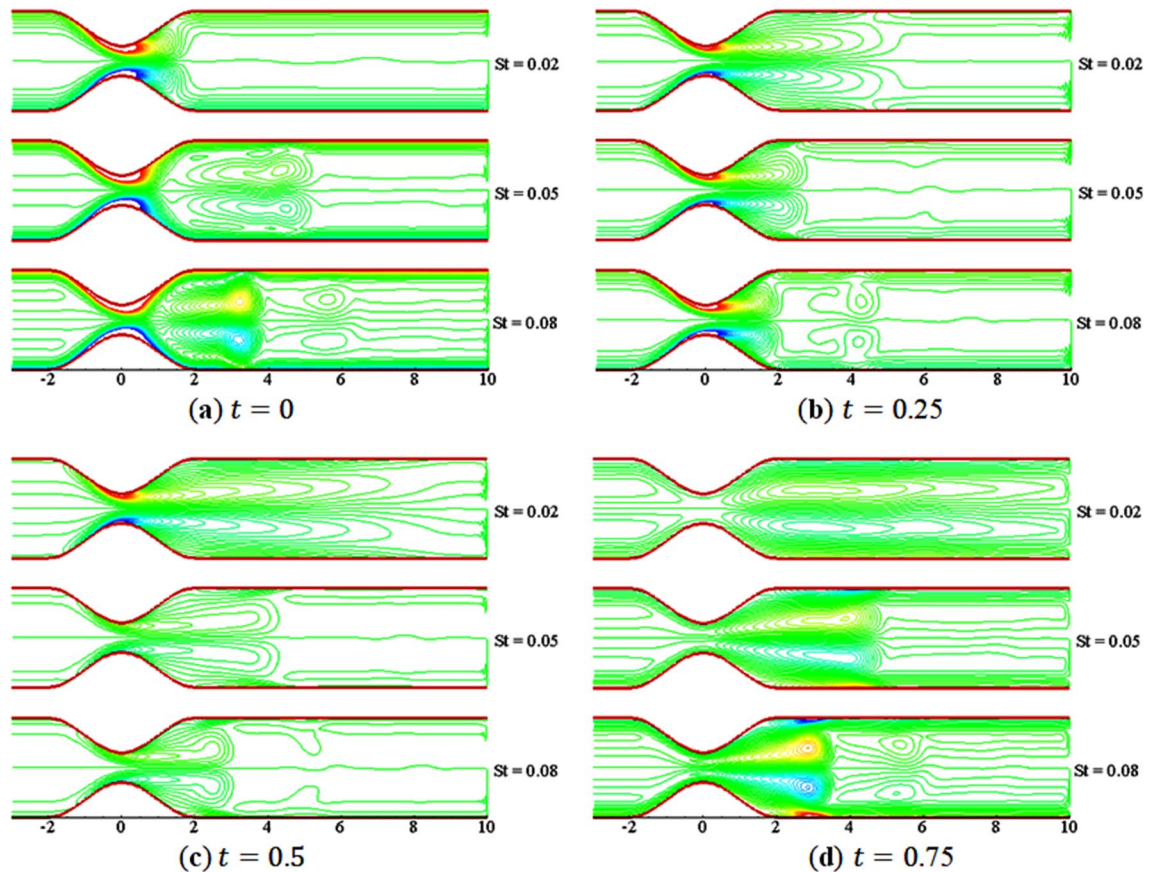


Figure 12. Vorticity contours for $St = 0.02, 0.05, 0.08$.

Data availability

The pictorial and graphical data used to support the findings of this study are included in the manuscript.

Received: 27 February 2020; Accepted: 29 May 2020

Published online: 30 June 2020

References

- Ochoa, M. V. *Analysis of Drilling Fluid Rheology and Tool Joint Effects to Reduce Errors in Hydraulics Calculation*. Ph.D. Thesis. (2006).
- Ellahi, R. Effects of the slip boundary condition on non-Newtonian flows in a channel. *Commun. Nonlinear Sci. Numer. Simulat.* **14**, 1377–1384 (2009).
- Ellahi, R. & Riaz, A. Analytical solutions for MHD flow in a third-grade fluid with variable viscosity. *Math. Comput. Model.* **52**, 1783–1793 (2010).
- Casson, N. A flow equation for the pigment oil suspension of the printing ink type. In *Rheology of Disperse Systems*. Pergamon. 84–102 (1959).
- Dash, R. K., Mehta, K. N. & Jayaraman, G. Casson fluid flow in a pipe filled with a homogeneous porous medium. *Int. J. Eng. Sci.* **34**, 1145–1156 (1996).
- Vardanyan, V. A. Effect of magnetic field on blood flow. *Biofizika* **18**, 491–496 (1973).
- Blair, G. W. S. An equation for the flow of blood, plasma and serum through glass capillaries. *Nature* **183**, 613–614 (1959).
- Charm, S. & Kurland, G. Viscometry of human blood for shear rates of 0–100,000 sec^{-1} . *Nature* **206**, 617–618 (1965).
- Sarifuddin. CFD modelling of Casson fluid flow and mass transport through atherosclerotic vessels. *Differ. Equ. Dyn. Syst.* (2020).
- Siddiqui, S. U., Verma, N. K., Mishra, S. & Gupta, R. S. Mathematical modelling of pulsatile flow of Casson's fluid in arterial stenosis. *Appl. Math. Comput.* **210**, 1–10 (2009).
- Priyadarshini, S. & Ponalagusamy, R. Mathematical modelling for pulsatile flow of Casson fluid along with magnetic nanoparticles in a stenosed artery under external magnetic field and body acceleration. *Neural Comput. Appl.* **31**, 813–826 (2019).
- Fredrickson, A. G. *Principles and Applications of Rheology* (Prentice-Hall, London, 1964).
- Mustafa, M., Hayat, T., Pop, I. & Aziz, A. Unsteady boundary layer flow of a Casson fluid due to an impulsively started moving flat plate. *Heat Transf.-Asian Res.* **40**, 563–576 (2011).
- Hayat, T., Sajid, M. & Pop, I. Three-dimensional flow over a stretching surface in a viscoelastic fluid. *Nonlinear Anal. Real World Appl.* **9**, 1811–1822 (2008).
- Pramanik, S. Casson fluid flow and heat transfer past an exponentially porous stretching surface in presence of thermal radiation. *Ain Shams Eng. J.* **5**, 205–212 (2014).
- Khan, A. et al. MHD flow of sodium alginate-based Casson type nanofluid passing through a porous medium with Newtonian heating. *Sci. Rep.* **8**, 8645 (2018).
- Kumar, K. G., Gireesha, B. J. & Manjunatha, S. Scrutinization of Joule heating and viscous dissipation on MHD flow and melting heat transfer over a stretching sheet. *Int. J. Appl. Mech. Eng.* **23**, 429–443 (2018).

18. Kumar, K. G., Gireesha, B. J., Krishnamurthy, M. R. & Prasannakumara, B. C. Impact of convective condition on Marangoni convection flow and heat transfer in Casson nanofluid with uniform heat source sink. *J. Nano.* **7**, 108–114 (2018).
19. Kumar, K. G., Gireesha, B. J., Prasannakumara, B. C. & Makinde, O. D. Impact of chemical reaction on Marangoni boundary layer flow of a Casson nano liquid in the presence of uniform heat source sink. *Adv. Nonlinear Heat Transf. Fluids Solids* **11**, 22–32 (2017).
20. Kumar, K. G., Archana, M., Gireesha, B. J., Krishnamurthy, M. R. & Rudraswamy, N. G. Cross diffusion effect on MHD mixed convection flow of nonlinear radiative heat and mass transfer of Casson fluid over a vertical plate. *Results Phys.* **8**, 694–701 (2018).
21. Gireesha, B. J., Kumar, K. G., & Manjunatha, S. Impact of chemical reaction on MHD 3D flow of a nanofluid containing gyrotactic microorganism in the presence of uniform heat source/sink. *Int. J. Chem. React. Eng.* **16** (2018).
22. Kumar, K. G., Gireesha, B. J., Krishnamurthy, M. R., Manjunatha, S. & Rudraswamy, N. G. Impact of ohmic heating on MHD mixed convection flow of Casson fluid by considering cross diffusion effect. *Nonlinear Eng.* **8**, 380–388 (2019).
23. Nourazar, S. S., Nazari-Golshan, A. & Soleymanpour, F. On the expedient solution of the magneto-hydrodynamic Jeffery-Hamel flow of Casson fluid. *Sci. Rep.* **8**, 16358 (2018).
24. Reddy, M. G., Vijayakumari, P., Sudharani, M. V. N. L., & Kumar, K. G. Quadratic convective heat transport of Casson nanoliquid over a contract cylinder: An unsteady case. *Nature* (2019).
25. Debnath, S. *et al.* Transport of a reactive solute in a pulsatile non-Newtonian liquid flowing through an annular pipe. *J. Eng. Math.* **116**, 1–22 (2019).
26. Khan, D. *et al.* Effects of relative magnetic field, chemical reaction, heat generation and Newtonian heating on convection flow of Casson fluid over a moving vertical plate embedded in a porous medium. *Sci. Rep.* **9**, 400 (2019).
27. Amlimohamadi, H., Akram, M. & Sadeghy, K. Flow of a Casson fluid through a locally-constricted porous channel: A numerical study. *Korea-Aust. Rheol. J.* **28**, 129–137 (2016).
28. Ali, F., Ahmad, N. S., Khan, I. & Saqib, M. Magnetic field effect on blood flow of Casson fluid in axisymmetric cylindrical tube: A fractional model. *J. Magn. Magn. Mater.* **423**, 327–336 (2017).
29. Hameed, M. & Nadeem, S. Unsteady MHD flow of a non-Newtonian fluid on a porous plate. *J. Math. Anal. Appl.* **325**, 724–733 (2007).
30. Misra, J. C., Shit, G. C., Chandra, S. & Kundu, P. K. Hydromagnetic flow and heat transfer of a second-grade viscoelastic fluid in a channel with oscillatory stretching walls: Application to the dynamics of blood flow. *J. Eng. Math.* **69**, 91–100 (2011).
31. Prasad, K. V., Vajravelu, K., Shivakumara, I. S., Vaida, H. & Basha, N. Z. Flow and heat transfer of a Casson nanofluid over a nonlinear stretching sheet. *J. Nano.* **5**, 743–752 (2016).
32. Bandyopadhyay, S. & Layek, G. C. Study of magnetohydrodynamic pulsatile flow in a constricted channel. *Commun. Nonlinear Sci. Numer. Simulat.* **17**, 2434–2446 (2012).
33. Hayat, T., Shehzad, S. A. & Alsaedi, A. Soret and Dufour effects on magnetohydrodynamic (MHD) flow of Casson fluid. *Appl. Math. Mech.-Engl. Ed.* **33**, 1301–1312 (2012).
34. Eldabe, N. T. M. & Salwa, M. G. E. Heat transfer of MHD non-Newtonian Casson fluid flow between two rotating cylinders. *J. Phys. Soc. Jpn.* **64**, 41–64 (1995).
35. Ali, A. & Syed, K. S. An outlook of high performance computing infrastructures for scientific computing. *Adv. Comput.* **91**, 87–118 (2013).

Acknowledgements

The authors are thankful to Computing Research and Development Center (CRDC) at Institute of Computing, Bahauddin Zakariya University, Multan, Pakistan for providing access to one of their SMP/multicore machine for execution of the code.

Author contributions

A.A. and Z.A. designed the Study. H.F. and A.A. developed the software for the study. Z.B. and A.F. conducted the experiments and sketched the plot. A.A., Z.A., and Z.B. wrote the paper. A.A., Z.A. H.F. provided the general assistance. All authors reviewed the manuscript.

Competing interests

The authors declare no competing interests.

Additional information

Correspondence and requests for materials should be addressed to A.A.

Reprints and permissions information is available at www.nature.com/reprints.

Publisher's note Springer Nature remains neutral with regard to jurisdictional claims in published maps and institutional affiliations.



Open Access This article is licensed under a Creative Commons Attribution 4.0 International License, which permits use, sharing, adaptation, distribution and reproduction in any medium or format, as long as you give appropriate credit to the original author(s) and the source, provide a link to the Creative Commons license, and indicate if changes were made. The images or other third party material in this article are included in the article's Creative Commons license, unless indicated otherwise in a credit line to the material. If material is not included in the article's Creative Commons license and your intended use is not permitted by statutory regulation or exceeds the permitted use, you will need to obtain permission directly from the copyright holder. To view a copy of this license, visit <http://creativecommons.org/licenses/by/4.0/>.

© The Author(s) 2020